Frequency- and Phase-Tunable Coupler Based on Three-Line and Four-Line Coupled Lines

Bo Huang*, Yongle Wu, Shuchen Zhen, Weimin Wang, and Jinchun Gao

School of Integrated Circuits, Beijing University of Posts and Telecommunications, Beijing, China

ABSTRACT: This paper proposes a reconfigurable 3-dB coupler with tunable phase and frequency characteristics based on triple-line loaded varactor diodes. The core structure employs a four-line coupling configuration to ensure strong coupling characteristics and stability. Through integrated theoretical analysis and experimental verification, the coupler demonstrates a center frequency tuning range of 1.8–2.4 GHz with continuous phase difference adjustment from 40° to 140°. Measured results indicate that high isolation (> 20 dB) and low return loss (< -20 dB) can be obtained.

1. INTRODUCTION

The rapid advancement of wireless communication technologies has imposed stringent requirements on microwave components and radio frequency (RF) circuits. Conventional devices such as couplers [1], power dividers [2], and filters [3] increasingly fail to meet modern communication systems' demands for multiband and multimode operations [4]. Furthermore, wireless power transfer (WPT) systems also impose corresponding requirements on frequency and phase reconfigurability. For example, efficient WPT systems rely on real-time frequency and phase adjustment to avoid energy loss [5]. The industry now prioritizes environmental adaptability, requiring components to dynamically adjust operating frequency, power division ratio, and phase difference for optimal performance across diverse scenarios. Consequently, reconfigurable devices [6–9] have emerged as a critical research focus.

As pivotal components in multiband wireless systems, hybrid couplers [10–13] require tunable parameters including power division ratio, phase difference, and center frequency, or even multifunctional adjustability [14]. The primary design challenge lies in expanding the tuning ranges of these parameters while preserving essential performance metrics such as isolation and amplitude balance.

Recent advancements in tunable coupler design have seen several innovative approaches. As documented in [15], researchers developed a novel vertically installed planar (VIP) structure that significantly expands frequency tuning ranges. Building upon the foundational research on frequency adaptivity, Ref. [16] significantly enhanced phase control capabilities by proposing a tunable directional coupler structure capable of achieving continuous phase adjustment from 45° to 135° while maintaining constant amplitude characteristics. Ref. [17] realized frequency-reconfigurable operation through the implementation of a frequency-reconfigurable matching network

(MN). Structural innovations are exemplified by [18], where reconfigurable units replace conventional $\lambda/4$ or $3\lambda/4$ transmission lines, thereby enabling switchable coupling paths and concurrent tuning of both frequency and power ratios. Multiband operation has been effectively addressed by the tri-band coupler proposed in [19], which achieves three independently tunable frequencies. Such advancements collectively demonstrate the field's progress toward multifunctional adaptability, while revealing ongoing challenges in maintaining balanced performance metrics.

This work presents an improved tunable coupler design. Departing from the dual-line configuration in [20], our design employs a triple-line structure to replace conventional dual-line tuning sections. Quadrilateral closed-loop configurations at both ends ensure 3-dB strong coupling. Through optimized electrical length ratios and impedance matching between tuning and main coupling sections, this design significantly enhances key performance metrics while retaining tunability. This work offers novel insights for tunable coupler design and lays a technical foundation for future RF front-end integration.

2. THEORY AND DESIGN

The proposed phase- and frequency-tunable coupler is illustrated in Figure 1. This configuration fundamentally comprises two quad-line coupled-line sections and two varactor-loaded tri-line tuning sections. Since the triple-line varactor-loaded structure is a multi-conductor coupled asymmetric system, conventional odd-even mode analysis is inapplicable to this structure. Consequently, independent analyses are first performed on the triple-line varactor-loaded tuning section and quad-line coupled-line section. Subsequently, for the convenience of theoretical analysis, this research investigates the frequency and phase tunability based on a simplified ideal structure.

This paper adopts the following assumptions and symbol definitions. Assumptions: Transmission lines are lossless; varac-

---
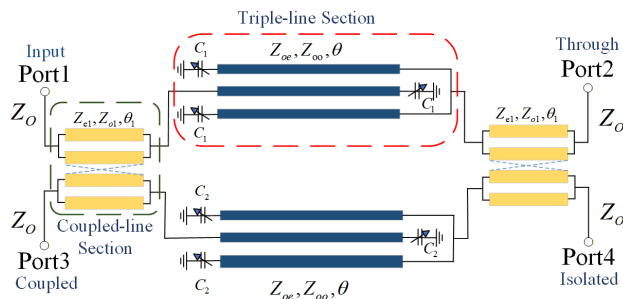
FIGURE 1. The proposed tunable hybrid coupler model based on a triple-line loaded diode configuration.
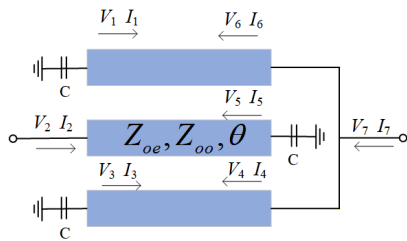
FIGURE 2. Triple-coupled line loaded with varactor diodes.

tor diodes are treated as pure capacitors; and the port characteristic impedance $Z_0 = 50\,\Omega$. Symbols: Z_{oe}/Z_{oo} denotes the even-mode/odd-mode characteristic impedance of the three-line coupled section; Z_{e1}/Z_{o1} denotes the even-mode/odd-mode characteristic impedance of the four-line coupled section; θ_1/θ denotes the electrical length; $Z_T = 1/(j\omega C)$ is the varactor diode impedance, where C_1/C_2 is regulated by the bias voltage.

2.1. Analysis of Diode-Loaded Triple-Coupled Lines

The impedance matrix (Z-parameter matrix) of a conventional triple-line coupled six-port network is given in [21, 22]. Equation (1) is the Z-parameter matrix of the three-line coupled six-port network, describing the mutual impedance between lines. Its elements consist of trigonometric terms of odd-even mode impedance and electrical length, reflecting the coupling phase characteristics. Symbol: k_{cc} denotes the ratio of coupling coefficients between non-adjacent and adjacent lines in the triple-line coupled structure.

$$\begin{pmatrix} V_1 \\ V_2 \\ V_3 \\ V_4 \\ V_5 \\ V_6 \end{pmatrix} = \begin{pmatrix} Ea & Fa & Ga & G\beta & F\beta & E\beta \\ Fa & Ea & Fa & F\beta & E\beta & F\beta \\ Ga & Fa & Ea & E\beta & F\beta & G\beta \\ G\beta & F\beta & E\beta & Ea & Fa & Ga \\ F\beta & E\beta & F\beta & Fa & Ea & Fa \\ E\beta & F\beta & G\beta & Ga & Fa & Ea \end{pmatrix} \begin{pmatrix} I_1 \\ I_2 \\ I_3 \\ I_4 \\ I_5 \\ I_6 \end{pmatrix} \quad (1)$$

where

$$\begin{cases} Ea = [-j\,(Z_{oe} + Z_{oo})\cot\theta]/2 \\ Fa = [-j\,(Z_{oe} - Z_{oo})\cot\theta]/2 \\ E\beta = [-j\,(Z_{oe} + Z_{oo})\csc\theta]/2 \\ F\beta = [-j\,(Z_{oe} - Z_{oo})\csc\theta]/2 \\ Ga = [-jk_{cc}\,(Z_{oe} - Z_{oo})\cot\theta]/2 \\ G\beta = [-jk_{cc}\,(Z_{oe} - Z_{oo})\csc\theta]/2 \end{cases} \quad (2)$$

The analysis of the varactor-loaded triple-coupled line in Figure 2 is as follows: The resultant port matrix is derived by solving port conditions and the six-port impedance matrix (Z-matrix) simultaneously. Equation (3) is the port constraint condition for varactor loading. $V_1 = -Z_T I_1$ describes the voltage-current relationship of the varactor, and $I_7 = I_4 + I_6$ is derived from Kirchhoff's Current Law (KCL).

$$\begin{cases} V_1 = -Z_T I_1 \\ V_3 = -Z_T I_3 \\ V_5 = -Z_T I_5 \\ V_4 = V_7 = V_6 \\ I_7 = I_4 + I_6 \\ Z_T = 1/(j\omega C) \end{cases} \quad (3)$$

The varactor-loaded three-line coupled structure is analyzed as follows: the port constraint conditions are restated in Equation (3). Substituting these constraint conditions into the six-port Z-parameter matrix and eliminating irrelevant port currents/voltages yields the two-port Z-parameter matrix Z_{tri} (Equations (4)/(4a)), from which the three-line coupled structure's Z-parameters Z_{tri1} (Equation (5)) are derived. Subsequently, the new $ABCD$ matrix M_1 is derived from Z_{tri1}.

$$Z_{tri} = \begin{pmatrix} Z_{11} & Z_{12} \\ Z_{21} & Z_{22} \end{pmatrix} \quad (4)$$

$$Z_{11} = -\frac{1}{2}j(Z_{oe} + Z_{oo})$$

$$\cot\theta\left(1 + \frac{2\,(-2j(Z_{oe}+Z_{oo})Z_T+\mathrm{Num1})\csc 2\theta}{\mathrm{Den1}}\right.$$

$$\left.-\frac{4(Z_{oe}-Z_{oo})^2\mathrm{Num3}}{(Z_{oe}+Z_{oo})\mathrm{Den2}}\right),$$

$$Z_{12} = -\frac{1}{2}j(Z_{oe} - Z_{oo})$$

$$\csc\theta\left(1 + \frac{(Z_{oe}+Z_{oo})(k_{cc}(Z_{oe}-Z_{oo})+\mathrm{Num3})}{\mathrm{Den1}}\right.$$

$$\left.+\frac{2\cot\theta(2j\mathrm{Num2}Z_T-\mathrm{Num1})}{\mathrm{Den2}}\right),$$

$$Z_{21} = -\frac{1}{2}j(Z_{oe} - Z_{oo})$$

$$\csc\theta\left(1 + \frac{\cot\theta\,(-2j(Z_{oe}+Z_{oo})Z_T+\mathrm{Num1})}{\mathrm{Den1}}\right.$$

$$\left.-\frac{2\mathrm{Num2}\mathrm{Num3}}{\mathrm{Den2}}\right),$$

$$Z_{22} = -\frac{1}{4}j\mathrm{Num2}$$

$$\cot\theta\left(1 + \frac{2(Z_{oe}-Z_{oo})^2(k_{cc}(Z_{oe}-Z_{oo})+\mathrm{Num3})}{\mathrm{Num2}\mathrm{Den1}}\right.$$

$$+\frac{4(2\mathrm{j}\mathrm{Num}2Z_T-\mathrm{Num}1)\csc 2\theta}{\mathrm{Den}2}\Bigg),$$

$$\mathrm{Den}1=-4Z_T^2+2\mathrm{j}((2+k_{cc})Z_{oe}-(-2+k_{cc})Z_{oo})Z_T\cot\theta$$
$$+(Z_{oe}+Z_{oo})(Z_{oe}+k_{cc}Z_{oe}+Z_{oo}-k_{cc}Z_{oo})\cot^2\theta$$
$$-2(Z_{oe}-Z_{oo})^2\csc^2\theta,$$
$$\mathrm{Den}2=8Z_T^2-4\mathrm{j}((2+k_{cc})Z_{oe}-(-2+k_{cc})Z_{oo})Z_T\cot\theta$$
$$-2(Z_{oe}+Z_{oo})(Z_{oe}+k_{cc}Z_{oe}+Z_{oo}-k_{cc}Z_{oo})\cot^2\theta$$
$$+4(Z_{oe}-Z_{oo})^2\csc^2\theta,$$
$$\mathrm{Num}1=(-(-1+k_{cc})Z_{oe}^2-6Z_{oe}Z_{oo}+(1+k_{cc})Z_{oo}^2)\cot\theta,$$
$$\mathrm{Num}2=(1+k_{cc})Z_{oe}+(1-k_{cc})Z_{oo},$$
$$\mathrm{Num}3=Z_{oe}+Z_{oo}-2\mathrm{j}Z_T\cot\theta \qquad (4\mathrm{a})$$

$$Z_{\mathrm{tri}1}=\begin{pmatrix} Z_{\mathrm{tri}} & 0 \\ 0 & Z_{\mathrm{tri}} \end{pmatrix} \qquad (5)$$

To simplify the analysis, when analyzing the four-line coupled structure in Figure 3, the coupling between the first line and third/fourth lines is first neglected [11]. Consequently, the first line is treated as part of a double-coupled line configuration, simplifying the analysis.
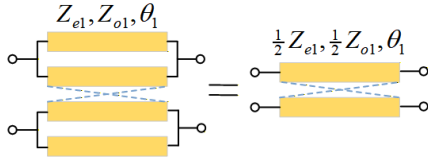
FIGURE 3. Four-coupled lines are equivalent to two-coupled lines.

The Z-parameters of the coupled lines are given by Equation (6). Its elements reflect how the even-mode/odd-mode impedance difference $(Z_{e1}-Z_{o1})$ and sum $(Z_{e1}+Z_{o1})$ affect the coupling strength and phase [20].

$$\begin{cases} Z_{11}=Z_{22}=Z_{33}=Z_{44}=[-\mathrm{j}\,(Z_{e1}+Z_{o1})\cot\theta_1]/4 \\ Z_{12}=Z_{21}=Z_{34}=Z_{43}=[-\mathrm{j}\,(Z_{e1}-Z_{o1})\cot\theta_1]/4 \\ Z_{13}=Z_{31}=Z_{24}=Z_{42}=[-\mathrm{j}\,(Z_{e1}-Z_{o1})\csc\theta_1]/4 \\ Z_{14}=Z_{41}=Z_{23}=Z_{32}=[-\mathrm{j}\,(Z_{e1}+Z_{o1})\csc\theta_1]/4 \end{cases} \qquad (6)$$

Using the equivalence of two coupled lines derived from the four-line coupled structure, Equation (7) gives the general expression for converting the four-port Z-parameters to the four-port $ABCD$ matrix [23]. The four-port network of the four-line coupled section is converted to a two-port cascaded matrix to facilitate subsequent cascading analysis. $Z_{ee}Z_{ie}^{-1}$: corresponds to the A-parameter of the $ABCD$ matrix, describing the voltage transmission relationship between the external and internal ports. $Z_{ee}Z_{ie}^{-1}$ corresponds to the $ABCD$ matrix's A-parameter, describing the voltage transmission relationship between external and internal ports. $Z_{ee}Z_{ie}^{-1}Z_{ii}-Z_{ei}$ corresponds to the B-parameter (transfer impedance) of the $ABCD$ matrix, describing the relationship between the external port voltage and the internal port reverse current. Z_{ie}^{-1} corresponds to the C-parameter (transfer admittance) of the $ABCD$ matrix, describing the relationship between the external port current and the internal port voltage. $Z_{ie}^{-1}Z_{ii}$ corresponds to the $ABCD$ matrix's D-parameter, describing the transmission relationship between the external port current and the internal port reverse current.

$$M_2=\begin{pmatrix} Z_{ee}Z_{ie}^{-1} & Z_{ee}Z_{ie}^{-1}Z_{ii}-Z_{ei} \\ Z_{ie}^{-1} & Z_{ie}^{-1}Z_{ii} \end{pmatrix} \qquad (7)$$

2.2. Frequency and Phase Difference Adjustable Analysis

For this coupler, the $ABCD$ matrices of the coupling section and intermediate tunable section are cascaded, where M_1 denotes the $ABCD$ matrix of the two triple-coupled line structures (Figure 1). The coupler's required S-parameters are then derived via S-parameter transformation.

Equation (8), $M_3 = M_2 \cdot M_1 \cdot M_2$, describes the cascaded configuration: "four-line coupled section (M_2) — three-line varactor-loaded section (M_1) — four-line coupled section (M_2)". Specifically, M_2 ensures the fundamental 3-dB coupling and phase reference (90° phase difference at the center frequency), while M_1 adjusts the equivalent electrical length and impedance via varactors. These tuning parameters are cascaded to synergize with M_1, enabling dual tuning of frequency (1.8–2.4 GHz) and phase (40°–140°).

$$M_3=M_2\cdot M_1\cdot M_2=\begin{pmatrix} A_2 & B_2 \\ C_2 & D_2 \end{pmatrix}\cdot\begin{pmatrix} A_1 & B_1 \\ C_1 & D_1 \end{pmatrix}\cdot\begin{pmatrix} A_2 & B_2 \\ C_2 & D_2 \end{pmatrix} \qquad (8)$$

Subsequently, the $ABCD$ matrix is converted to S-parameters (specifically S_{11}, S_{21}, S_{31}, and S_{41}) using the transformation method detailed in Chapter 2 of [23, 24]. The derived S-parameters enabled establishing correlations between operating frequency, phase difference, and varactor diodes' equivalent electrical length.

For a power division ratio of $R = 3\,\mathrm{dB}$, the phase difference is adjusted by inversely varying bias voltages V_1 and V_2 (with the center frequency kept constant), as per the phase tuning mechanism in [20]. Specifically, this approach uses the linear relationship $\theta_d = 2\theta_1$ (θ_d: output phase difference; θ_1: electrical length of the tunable transmission line), ensuring that the power division ratio remains unchanged during phase adjustment (since it is independent of θ_1).

For center frequency tunability, simultaneously increasing V_1 and V_2 adjusts the frequency, consistent with the frequency compensation strategy in [20]. This method dynamically tunes θ_1 to offset the frequency-dependent variation of the coupled-line electrical length θ_0, maintaining the core topological constraint $\theta_1 + \theta_2 = \theta_0 = 90°$ and ensuring stable quadrature phase difference across the operating frequency range.

This approach is verified via simulations and experimental measurements.
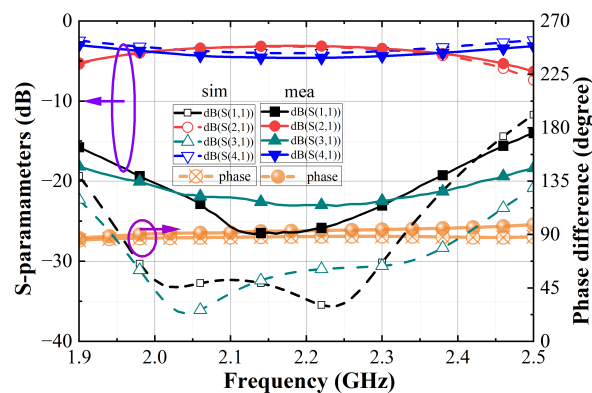
3. SIMULATION AND MEASUREMENT

To ensure the reliability of the theoretical results, we implemented a tunable hybrid coupler by following the design theory described herein and performed measurements to validate
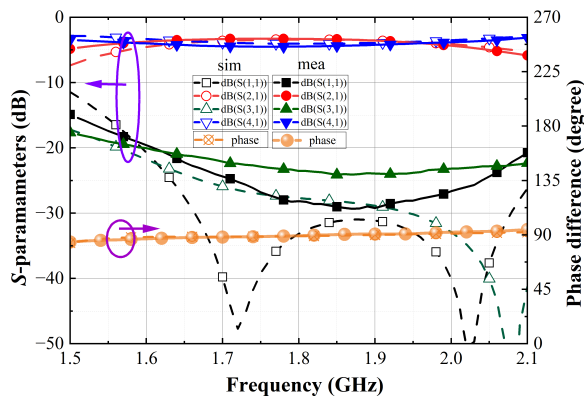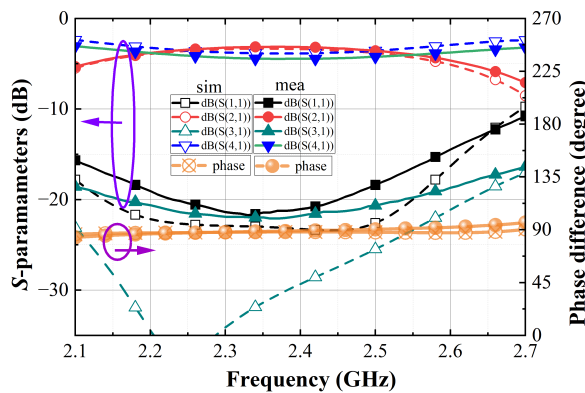
FIGURE 4. Simulation and measurement results of the designed tunable hybrid coupler at the center frequency of 1.8 GHz.
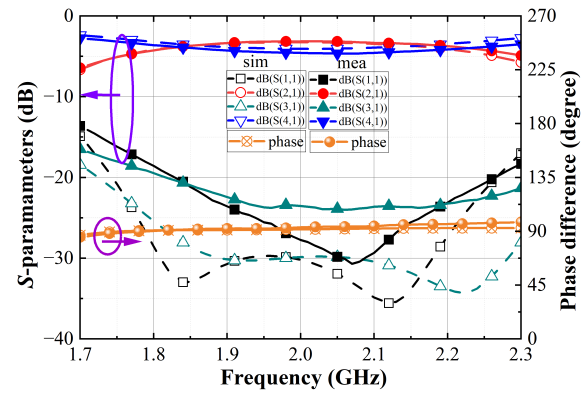
FIGURE 5. Simulation and measurement results of the designed tunable hybrid coupler at the center frequency of 2.0 GHz.

FIGURE 6. Simulation and measurement results of the designed tunable hybrid coupler at the center frequency of 2.2 GHz.

FIGURE 7. Simulation and measurement results of the designed tunable hybrid coupler at the center frequency of 2.4 GHz.

its performance. Figure 9 presents a photograph of the fabricated prototype, which was constructed on a RO4350B substrate with a dielectric constant of 3.66, substrate thickness of 1.524 mm, loss tangent (Tanδ) of 0.0035, and copper thickness (T) of 1.4 mil. The key parameters of the proposed coupler are as follows: $w_1 = 0.5$ mm, $w_2 = 0.6$ mm, $s_1 = 0.2$ mm, $s_2 = 0.15$ mm, $l_1 = 22$ mm, and $l_2 = 22$ mm (w_1, s_1 and l_1 represent the dimensions of the tripe-coupled lines, while w_2, s_2 and l_2 are used for the four-coupled lines). The varactor diode Skyworks SMV1265-011LF was employed as a tunable capacitor in this design, offering a capacitance range from 22.47 pF to 0.71 pF under a DC bias voltage varying between 0 V and 30 V. A 47 nH inductor served as an RF choke to prevent RF signal leakage into the DC path, while a 47 pF capacitor was utilized for DC blocking. The simulation of the proposed structure was conducted using Advanced Design System (ADS) 2023. A Rigol DP832A power supply was employed to provide bias voltage. The frequency-domain performance of the device was measured using a Rohde & Schwarz (R&S) ZVA8 vector network analyzer (VNA), with calibration implemented via an electronic calibration kit. Calibration was conducted over a frequency range of 1–3 GHz, with 201 frequency points (frequency step: 10 MHz) employed to ensure measurement accuracy across the target operating band.

Finally, Table 1 compares the performance metrics of reported reconfigurable couplers with our proposed design, highlighting the advantages of our work. In terms of RF performance, the return loss is < -20 dB and isolation > 20 dB, outperforming [15] (return loss < -10 dB, isolation > 10 dB), [19] (return loss < -12 dB, isolation > 12.5 dB), and [20] (return loss < -10 dB, isolation > 14 dB). Regarding tunability and phase range, unlike most designs that only support frequency tuning or fixed phase ([15, 17, 19, 25]), our design achieves dual frequency-phase tunability with a $40°$–$140°$ range that meets communication system demands. For frequency range applicability, its target band (1.8–2.4 GHz) covers mainstream applications and key WPT frequency bands. Compared to the broadband designs in [15] (1.3–2.7 GHz), [17] (1.0–2.96 GHz), and [20] (2.0–2.75 GHz, dual-coupled line structure), our design not only offers stronger specificity and higher practical value but also demonstrates superior RF performance compared to [20], while maintaining a high level of tunability.
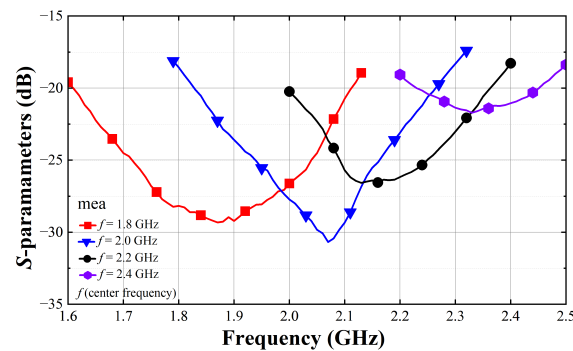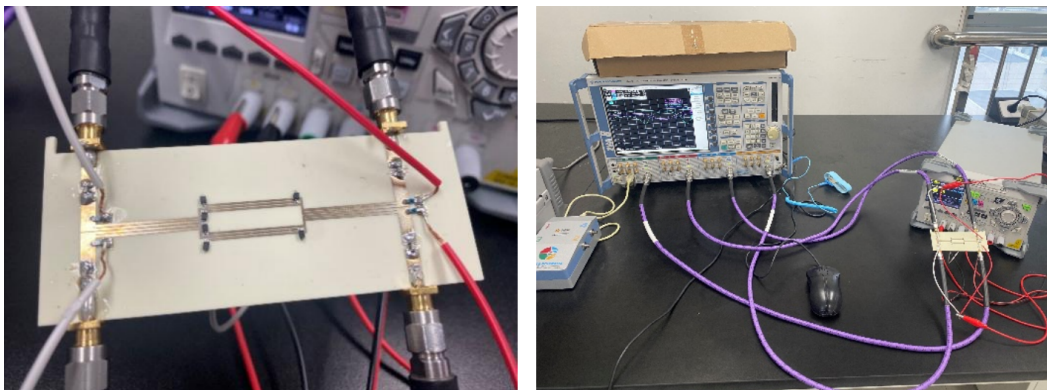
3.1. Tunable Frequency

The simulated and experimental results of the proposed coupler are as follows. In frequency-tuning mode, the power di-

TABLE 1. Comparison with published couplers.

References	Coupler Structure	Tunabilities	Frequency Range (GHz)	Phase Difference (Degree)	Return Loss (dB)	Isolation (dB)	Circuit Size (λg^2)
[15]	VIP	Frequency	1.3–2.7	Fixed	< -10	> 10	$0.32 * 0.18$
[17]	MN	Frequency	1.0–2.96	Fixed	< -20	> 35	$0.11 * 0.08$
[19]	Branch line	Independently Frequencies*3	1.3–1.5 2.3–3.0 3.9–4.3	Fixed	< -12	> 12.5	$0.25 * 0.5$
[20]	Coupled line	Frequency/Phase	2.0–2.75	$30°–150°$	< -10	> 14	$0.75 * 0.18$
[25]	Coupled line	Fixed (backward coupling functionality)	0.7–0.85	NA	NA	NA	$12\,\text{mm} \times 2.8\,\text{mm}$
This work	Coupled line	Frequency/Phase	1.8–2.4	$40°–140°$	< -20	> 20	$0.88 * 0.44$

Note: λg^2 denotes the squared guided wavelength; Reference [25] presents physical dimensions ($12\,\text{mm} \times 12\,\text{mm}$) as its original data did not provide λg^2-normalized values.

FIGURE 8. S_{11} at varying voltage levels (center frequency-tunable).

FIGURE 9. Measured photograph of the fabricated tunable hybrid coupler.

vision is maintained at 3 dB and the phase difference at 90°. Figures 4–7 show the simulated and measured frequency responses of the proposed coupler, with excellent agreement between simulation and measurement (phase difference refers to the phase shift between S_{21} and S_{31}). Figure 8 presents the measured S_{11} variation curves under different bias voltages, demonstrating the tunability of the center frequency. The device exhibits a return loss better than 20 dB, isolation greater than 20 dB, with additional insertion loss of 2 dB and output

phase imbalance within 5°. The center frequency is adjustable from 1.8 GHz to 2.4 GHz, maintaining a relative bandwidth of approximately 30% throughout the tuning range. The observed amplitude and phase imbalances are likely due to inaccuracies in varactor diode modeling. Specifically, the consistency between simulation and measurement results is relatively poor at 2.4 GHz, which may be further exacerbated by layout parasitic effects and environmental interference at the upper end of the frequency band.
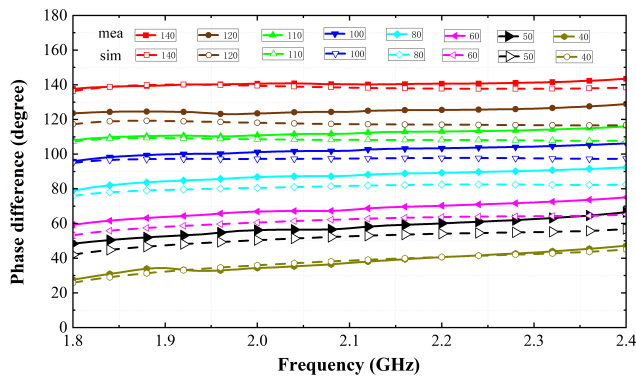
FIGURE 10. The simulation and measurement results of the designed tunable hybrid coupler with phase differences ranging from 40° to 140°.

3.2. Phase Difference Tuning

The simulated and experimental results of the phase difference tuning performance of the coupler are presented as follows. Under this tunable phase difference mode, the center frequency remains stable at 2.1 GHz while maintaining a 3-dB power division ratio. Figure 10 illustrates the simulated and measured phase difference responses of the proposed coupler. Excellent agreement is observed between simulations and measurements. The return loss better than 20 dB and isolation surpassing 20 dB, with 2-dB additional insertion loss are obtained. The phase difference can be continuously tuned from 40° to 140° within the 1.8–2.4 GHz range. Throughout the entire tuning range, the phase imbalance remains below 10° across the full passband.

4. CONCLUSION

This study presents, designs, and actualizes a novel tunable hybrid coupler grounded on an enhanced coupled-line configuration. By substituting the fixed dual-line structure in the middle with a newly developed triple-line tunable design and employing a main coupling section featuring a four-line closed structure at both ends to attain strong coupling, the crucial performance metrics are optimized while safeguarding the circuit's compactness.

Experimental findings demonstrate that the coupler can accomplish continuous frequency tuning within the 1.8–2.4 GHz range. At a center frequency of 2.1 GHz, within a 20 % relative bandwidth (roughly 1.8–2.4 GHz), the coupler enables continuous tunability of the phase difference from 40° to 140°. Moreover, it sustains excellent return loss (< -20 dB), isolation (> 20 dB) across the full tuning range.

The circuit structure is relatively uncomplicated and holds great potential for extensive application in multi-mode microwave and RF circuits.

ACKNOWLEDGEMENT

REFERENCES

[1] Chi, J.-G. and Y.-J. Kim, "A compact wideband millimeter-wave quadrature hybrid coupler using artificial transmission lines on a glass substrate," *IEEE Microwave and Wireless Components Letters*, Vol. 30, No. 11, 1037–1040, 2020.

[2] Sharma, K., B. Biswas, and S. K. Parui, "Design of a compact low loss four-way power divider at W-band," in *2023 7th International Conference on Electronics, Materials Engineering & Nano-Technology (IEMENTech)*, 1–5, Kolkata, India, 2023.

[3] Feng, W., X. Gao, W. Che, and Q. Xue, "Bandpass filter loaded with open stubs using dual-mode ring resonator," *IEEE Microwave and Wireless Components Letters*, Vol. 25, No. 5, 295–297, 2015.

[4] Zhang, Y., J. Pang, Z. Li, M. Tang, Y. Liao, A. A. Fadila, A. Shirane, and K. Okada, "A power-efficient CMOS multi-band phased-array receiver covering 24–71-GHz utilizing harmonic-selection technique with 36-dB inter-band blocker tolerance for 5G NR," *IEEE Journal of Solid-State Circuits*, Vol. 57, No. 12, 3617–3630, 2022.

[5] Guo, Z., F. Yang, H. Zhang, X. Wu, Q. Wu, K. Zhu, J. Jiang, H. Jiang, Y. Yang, Y. Li, and H. Chen, "Level pinning of anti-PT-symmetric circuits for efficient wireless power transfer," *National Science Review*, Vol. 11, No. 1, nwad172, Jan. 2024.

[6] Li, L., X. Yan, H. C. Zhang, and Q. Wang, "Polarization-and frequency-reconfigurable patch antenna using gravity-controlled liquid metal," *IEEE Transactions on Circuits and Systems II: Express Briefs*, Vol. 69, No. 3, 1029–1033, 2022.

[7] Fan, M., K. Song, L. Yang, and R. Gómez-García, "Frequency-tunable constant-absolute-bandwidth single-/dual-passband filters and diplexers with all-port-reflectionless behavior," *IEEE Transactions on Microwave Theory and Techniques*, Vol. 69, No. 2, 1365–1377, 2021.

[8] Wang, L., J. Chen, D. Hou, X. Xu, and R. Zhou, "A 2.9-8.4-GHz reconfigurable 90° coupler with compact size in 0.13-μm SiGe BiCMOS," *IEEE Microwave and Wireless Technology Letters*, Vol. 34, No. 3, 283–286, 2024.

[9] Li, H., X. Guo, T. Yu, L. Zhu, and W. Wu, "Wideband continuously tunable phase shifter with phase slope tunability and low phase error," *IEEE Transactions on Microwave Theory and Techniques*, Vol. 70, No. 4, 2147–2155, 2022.

[10] Ding, K. and A. Kishk, "Wideband hybrid coupler with electrically switchable phase-difference performance," *IEEE Microwave and Wireless Components Letters*, Vol. 27, No. 11, 992–994, 2017.

[11] Zheng, Y., Y. Wu, W. Wang, and L. Pan, "Uniplanar compact 180° hybrid coupler with fast and accurate wide power-division ratio switching ranges and enhanced bandwidth," *IEEE Transactions on Microwave Theory and Techniques*, Vol. 71, No. 12, 5470–5481, 2023.

[12] Yoon, H.-J. and B.-W. Min, "Two section wideband 90° hybrid coupler using parallel-coupled three-line," *IEEE Microwave and Wireless Components Letters*, Vol. 27, No. 6, 548–550, 2017.

[13] Vigneswaran, S., E. Kervé, N. Deltimple, R. Mathieu, and K. Vivien, "Twisted-shaped millimeter-wave hybrid couplers in 150 nm GaN technology for 5G applications," in *2025 IEEE/MTT-S International Microwave Symposium — IMS 2025*, 698–701, San Francisco, CA, USA, 2025.

[14] Yang, S., X. Wang, H. Zhu, and G. Lu, "A coupling-path reconfigurable quadrature coupler with wide range of tunable frequencies and power division ratios," *IEEE Transactions on Microwave Theory and Techniques*, Vol. 72, No. 6, 3530–3541, 2024.

[15] Pan, Y. F., S. Y. Zheng, Y. M. Pan, Y. X. Li, and Y. L. Long, "A frequency tunable quadrature coupler with wide tuning range of center frequency and wide operating bandwidth," *IEEE Transactions on Circuits and Systems II: Express Briefs*, Vol. 65, No. 7, 864–868, 2018.

[16] Zhu, H. and A. M. Abbosh, "A compact tunable directional coupler with continuously tuned differential phase," *IEEE Microwave and Wireless Components Letters*, Vol. 28, No. 1, 19–21, 2018.

[17] Tan, X., J. Sun, and F. Lin, "A compact frequency-reconfigurable rat-race coupler," *IEEE Microwave and Wireless Components Letters*, Vol. 30, No. 7, 665–668, 2020.

[18] Tan, X., Z. Ma, Y. Zhang, and R. Zhao, "A compact multifunctional reconfigurable coupler with quadrature and rat-race functions," *IEEE Transactions on Microwave Theory and Techniques*, Vol. 73, No. 7, 3722–3732, 2025.

[19] Xu, B. W., S. Y. Zheng, and W. Che, "Flexible tri-band coupler with three independently tunable frequencies," *IEEE Transactions on Microwave Theory and Techniques*, Vol. 72, No. 9, 5441–5454, 2024.

[20] Xu, B. W., S. Y. Zheng, W. M. Wang, Y. L. Wu, and Y. A. Liu, "A coupled line-based coupler with simultaneously tunable phase and frequency," *IEEE Transactions on Circuits and Systems I: Regular Papers*, Vol. 66, No. 12, 4637–4647, 2019.

[21] Yamamoto, S., T. Azakami, and K. Itakura, "Coupled strip transmission line with three center conductors," *IEEE Transactions on Microwave Theory and Techniques*, Vol. 14, No. 10, 446–461, 1966.

[22] Zhu, Y., J. Cai, W. Qin, W. Yang, and J. Chen, "Compact input-reflectionless balanced bandpass filter with flexible bandwidth using three-line coupled structure," *Frontiers of Information Technology & Electronic Engineering*, Vol. 24, No. 2, 314–326, 2023.

[23] Wu, Y., W. Wang, J. Yan, Y. Zheng, and R. Wu, *Fundamental Theory of Generalized N-Port Microwave Circuits and RF Chips Complex-Impedancee Networks*, Publishing House of Electronics Industry, iSBN 978-7-121-49427-7, Jan. 2025 (in Chinese).

[24] Zhu, L., S. Sun, and R. Li, *Microwave Bandpass Filters for Wideband Communications*, John Wiley & Sons, 2012.

[25] Guo, Z., J. Song, H. Jiang, and H. Chen, "Miniaturized backward coupler realized by the circuit-based planar hyperbolic waveguide," *Advanced Photonics Research*, Vol. 2, No. 8, 2100035, 2021.